Nano Research

Open Access

Research Article

Femtosecond laser ablation for fabrication of high resolution and multicolor perovskite nanocrystals light-emitting diodes

Zilong Lu, Feng Zhang ✉, Zihan Ren, Yuxiang Zhang, and Tianrui Zhai ✉

School of Physics and Optoelectronic Engineering, Beijing University of Technology, Beijing 100124, China

Cite this article: *Nano Research*, **2026**, *19*, 94908488. https://doi.org/10.26599/NR.2026.94908488

ABSTRACT: The development of perovskite nanocrystals (NCs) based light-emitting diodes (LEDs) are looking for new patterning technology, which is crucial for realization of high resolution and full color displays. Herein, femtosecond (fs) laser processing is introduced for fabrication of patterned and pixelated $CsPbBr_3$ and $CsPbI_3$ NCs films. The rapid removal of NCs in target area under fs laser radiation is demonstrated, proving the effectiveness of fs laser ablation for patterning of perovskite NCs. As a result, pixelated $CsPbI_3$ and $CsPbBr_3$ NCs films with pixels per inch (PPI) up to 1693 and clear boundaries are successfully obtained. Then, electroluminescent (EL) devices with bilayered emission layers ($CsPbBr_3$ and $CsPbI_3$ NCs) are fabricated for exploration of multicolor LEDs. Through understanding into the carrier recombination dynamics, the dominant red emissions in these EL devices are well explained. Finally, multicolor EL devices with green and red pixels are realized with one-step fs laser ablation on $CsPbI_3$ NCs because of their priority in carrier recombination. Moreover, the as-fabricated multicolor EL devices achieve a maximum luminance of 488 cd/m² and external quantum efficiency of 7.7%, demonstrating great potential of fs laser ablation towards pixelated full color perovskite NCs based LEDs.

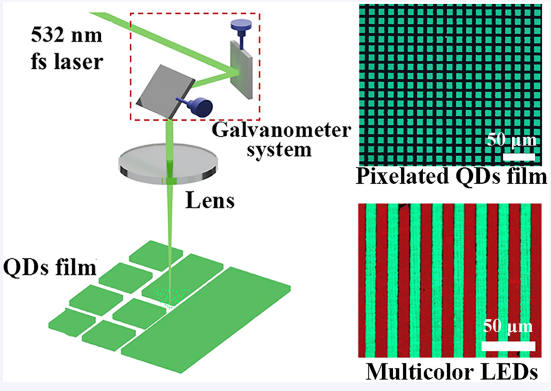

KEYWORDS: nanocrystals, perovskites, laser ablation, pixelation, light-emitting diodes

1 Introduction

Display technologies based on colloidal quantum dots (QDs) or nanocrystals (NCs) have been proposed and developed for nearly thirty years [1–4]. The unique size-tunable emissions, high luminescence efficiency, and solution-processability are main features for colloidal QDs, which enable them to be promising candidate whether in phosphor converted light-emitting diodes (LEDs) or in electrically driven LEDs [5–8]. As a new member of QDs family, perovskite QDs (PeQDs) are widely known and attract tremendous interest since the establishment of controllable solution fabrication process (hot-injection and ligand-assisted reprecipitation) in 2015 [9, 10]. Apart from the above characteristics, PeQDs are also superiority in high color purity and low-cost room temperature synthesis, showing great potential in next generation ultrawide color gamut displays [11–13]. In recent years, PeQDs based LEDs have witnessed significant development with external quantum efficiency (EQE) rapidly increasing to over 25% [14–16]. Despite for booming in EQE, exploration on QDs based LEDs towards multi-color and pixelation is still in the preliminary stage, which is crucial for further development and commercialization of QDs based LEDs [17, 18].

Realization of pixelated display requires controllable and precise patterning technology on emission layer consisted by QDs. Currently, the patterning technologies for QDs mainly include inkjet printing [19, 20], photolithography [21, 22], and micro/nano imprinting [23–25]. The inkjet printing raises high requirements for ink preparation. Moreover, the pixel size of inkjet printing is limited by the size of ejected droplets, resulting in relatively larger pixel size with low resolution [26, 27]. Photolithography and nanoimprinting are dependent on template which directly determines the pixel size and pattern. Photoresist residues, contact pollution, and template costs are unavoidable drawbacks for nanoimprinting and photolithography [28]. Ultrafast laser ablation, known as removing of materials from the surface through evaporation under high pulse energies, has been widely applied in

Received: November 3, 2025; **Revised:** January 19, 2026
Accepted: January 24, 2026

✉Address correspondence to Feng Zhang, fengzhang@bjut.edu.cn; Tianrui Zhai, trzhai@bjut.edu.cn

varied material systems [29–31]. Compared to continuous wave lasers, incredibly high optical energy can be precisely delivered to target area on a timescale much faster than heat diffusion in case of ultrafast lasers especially for femtosecond (fs) lasers [32]. With assistance of electrical/mechanical technologies, the highest processing speed can approach several meters per second level [33–35]. These features allow fs laser ablation as an efficient and mask-free micro-nano manufacturing technique with high spatial resolution (0.1–1 μm) [36]. Actually, treatment on perovskite crystals utilizing laser processing has been reported in a few studies such as fabrication of perovskite based micro-LEDs through continuous laser direct writing (LDW) [37, 38]. The physical mechanism of LDW for patterning on perovskite films mainly refers to thermal quenching or decomposition of perovskites under laser radiation. Incomplete decomposition of perovskites under moderate laser power always leads to formation of residual complicated oxide structures after LDW treatment. Owing to the significantly high peak power, fs laser ablation can be expected to be a promising solution for achieving high-quality patterned QDs film.

For multicolor LEDs, employing multicolored QDs in a single electroluminescent (EL) device is indispensable theoretically. Unfortunately, the simple overlap of different PeQDs as multiple emission layers would face unavoidable ion migration issue during operation, which seriously interferes with the color purity [39–41]. On the other hand, because of relatively constant mobility of electrons and holes in a certain device structure, recombination of electrons and holes may only occur within a small region [42]. Thus, it is difficult to achieve multicolor emissions from different QDs because the recombination cannot occur in all emission layers. Based on above analysis, the separation of different QDs in device structure, which can provide independent carrier injection channel for QDs, is essential for realization of multicolor LEDs [43]. However, establishing separate injection channels for QDs with different colors needs repeatably patterning on each QDs layer and subsequent accurate alignment, leading to complicated fabrication process [44, 45]. Therefore, exploration on one-step patterning without alignment technique is significance for multicolor LEDs.

In this paper, fs laser ablation is introduced for fabrication of pixelated $CsPbBr_3$ and $CsPbI_3$ NCs films. By adjusting the repetition, processing speed, and power of fs laser, $CsPbBr_3$ and $CsPbI_3$ NCs films with tunable pixel sizes and highest pixels per inch (PPI) up to 1693 are successfully obtained. The rapid evaporation of NCs under fs laser radiation, which is identified by elemental characterization, confirms the achievement of fs laser ablation and explains the processing mechanism of fs laser. Prototype devices with two emission layers are subsequently fabricated to further explore the carrier injection and transportation dynamics. Through analysis on transportation properties of electrons and holes as well as understanding into device energy level structure, dominant red emissions from $CsPbI_3$ NCs are well explained whether $CsPbI_3$ NCs layer is above or below $CsPbBr_3$ NCs layer. Due to the preferential red emission in multi-emission-layer devices, multicolor EL emissions are realized when fs laser ablation is only conducted on $CsPbI_3$ layer, bringing great convenience for achieving full color LEDs. Moreover, the as-fabricated multicolor EL devices show high resolution and maximum luminance of 488 cd/m^2 and EQE up to 7.7%. Our exploration brings great convenience for fabrication of multicolor and pixelated EL devices based on PeQDs, which may provide a new solution towards full color and high definition LEDs and further promote the development of PeQDs based displays.

2 Results and discussion

All inorganic $CsPbBr_3$ and $CsPbI_3$ NCs were fabricated through small modifications on hot-injection strategy (Detailed fabrication process can be referred to the Electronic Supplementary Material (ESM)). As shown in Fig. 1(a), as-fabricated $CsPbBr_3$ and $CsPbI_3$ NCs show bright green and red emissions in colloidal solutions. The obtained $CsPbBr_3$ and $CsPbI_3$ NCs exhibit characteristic crystal structure of PeQDs with high crystallinity confirmed by X-ray diffraction results (see Fig. S1 in the ESM). The average crystal size of $CsPbBr_3$ and $CsPbI_3$ NCs is 13.9 and 14.4 nm, respectively (see Fig. S2 in the ESM). Besides, as-fabricated $CsPbBr_3$ and $CsPbI_3$ NCs present narrow photoluminescence (PL) emissions centered at 522 and 656 nm as well as obvious excitonic absorption features, which are typical optical properties for $CsPbBr_3$ and $CsPbI_3$ NCs (see Fig. S3 in the ESM). Owing to the good dispersibility and high concentration, the as-fabricated $CsPbBr_3$ and $CsPbI_3$ NCs in colloidal solution can be well spin cast into high-quality thin films with bright PL emissions maintained, as shown in Fig. 1(a). Then, fs laser radiation is applied on the obtained $CsPbBr_3$ and $CsPbI_3$ NCs in order to explore the processing parameters towards pixelated NCs films. As shown in Fig. 1(b), an fs laser with wavelength of 532 nm, repetition rate of 5 kHz, and pulse width of 150 fs is used as laser source. The average power and scanning rate of the fs laser are adjusted to explore the suitable parameters. In the case of $CsPbBr_3$ NCs film, discrete pores with radius about 5 μm are observed under fluorescence microscope when using fs laser with average power of 3 mW and scanning rate of 60 mm/s, as shown in Fig. S4(a) in the ESM. According to the scanning rate and repetition of fs laser, it can be easily found that each pore observed in NCs film is created by a single pulse of fs laser. With the power increasing to 5 mW, these discrete pores connect together to form a continuous line (Fig. S4(b) in the ESM). However, the line width is also increased with the power increasing. When slowing down the processing rate to 20 or 30 mm/s at 3 mW, a clear straight line is formed on NCs film with line width maintained at 5 μm. Through further controlling the scanning path of fs laser by galvanometer system, $CsPbBr_3$ NCs film with varied patterns can be fabricated. Similar results are also demonstrated for $CsPbI_3$ NCs film (see Fig. S5 in the ESM). To reveal the processing mechanism of fs laser, $CsPbBr_3$ NCs film is manufactured into a patterned structure with periodic parallel stripes and analyzed by scanning electron microscopy (SEM) equipped with energy dispersive spectrometer (EDS). As SEM image and corresponding EDS mapping results of Cs, Pb, and Br show in Fig. 1(c), the distributions of Cs, Pb, and Br elements are in good agreement with the untreated areas observed in the SEM image. The nearly undetectable Cs, Pb, and Br elements in processed area imply that $CsPbBr_3$ NCs are totally removed after fs laser treatment. Considering the average power of 3 mW, pulse duration of 150 fs, and repetition frequency of 5 kHz, the instantaneous power of a single pulse is as high as 4×10^6 W. Under such high power, it can be reasonably considered that NCs experience rapid vaporization from the thin film. The fast removal of NCs under fs radiation well elucidates the occurrence of fs laser ablation, which makes fs laser a powerful processing technique for patterning of PeQDs. As a result, pixelated $CsPbBr_3$ NCs films with varied pixel sizes are fabricated. As shown in Figs. 1(d)–1(g), these films show uniformly arranged pixels and clear boundaries. The almost straight and flat boundary between treated and untreated area is further verified through SEM image under high magnification (see Fig. S6 in the ESM). Moreover, the PPI of these

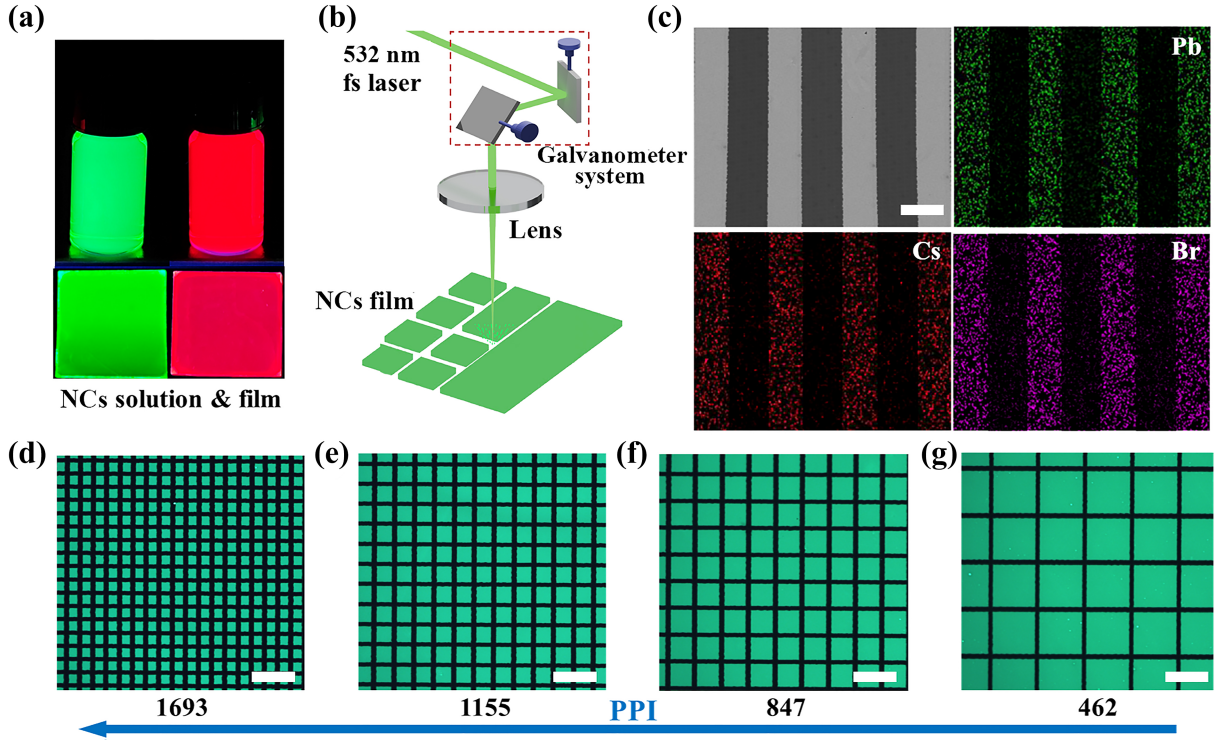

Figure 1 fs laser ablation for pixelated perovskite NCs films. (a) Photographs of $CsPbBr_3$ and $CsPbI_3$ NCs colloidal solutions and corresponding thin films. (b) Schematic illustration of fs laser processing on NCs. (c) SEM image of typical $CsPbBr_3$ NCs film and corresponding EDS mapping on Cs, Pb, and Br elements. The scale bar is 10 μm. (d)–(g) Images of pixelated $CsPbBr_3$ NCs films with varied pixel sizes captured by fluorescent confocal microscopy. The scale bar is 50 μm. Corresponding PPI are labeled at the bottom.

films can be determined from 462 to 1693, showing great potential of fs laser ablation for high resolution displays.

EL devices based on $CsPbI_3$ and $CsPbBr_3$ NCs are firstly fabricated using device structure of indium tin oxide (ITO)/poly(3,4-ethylene dioxythiophene):poly(styrene sulfonate) (PEDOT:PSS)/poly[bis(4-phenyl)(2,4,6-trimethylphenyl)amine] (PTAA)/NCs/1,3,5-tris(1-phenyl-1H-benzimidazol-2-yl)benzene (TPBi)/Al. As shown in Fig. S7 in the ESM, EL devices based on $CsPbI_3$ and $CsPbBr_3$ NCs show pure red and green emissions with maximum EQE of 1.7% and 11.5%, demonstrating the applicability of as-fabricated NCs in LEDs. For exploration of multicolor LEDs, prototype EL devices with two emission layers (simply overlapping of $CsPbBr_3$ and $CsPbI_3$ NCs layers) are fabricated using the same device structure as for single emission layer device. Besides, a thin layer of polymethyl methacrylate (PMMA, about 5 nm) is inserted between $CsPbBr_3$ and $CsPbI_3$ NCs as an insulating layer to prevent ion migration and film destruction by solvent [46]. As shown in Figs. 2(a) and 2(b), the relative position of $CsPbBr_3$ and $CsPbI_3$ layers in the device structure is exchanged. For convenience, EL device with $CsPbBr_3$ on top of $CsPbI_3$ is denoted as G/R type, while that with $CsPbI_3$ on top of $CsPbBr_3$ is denoted as R/G type. When exceeding the turn-on voltage, both R/G type and G/R type devices exhibit obvious red emissions centered at 653 nm, as demonstrated by EL spectra shown in Figs. 2(c) and 2(d). These observed red emissions maintain the same feature with PL of $CsPbI_3$ NCs, which clearly proves that they are originated from $CsPbI_3$ NCs. From the current density–voltage (*J*–*V*) curves shown in Fig. 2(e), device G/R shows lower current density than device R/G throughout the entire operation voltage. Lower turn-on voltage, higher maximum luminance, and superior device efficiency are also demonstrated for device G/R, as indicated by the luminance–voltage (*L*–*V*) and EQE curves shown in Fig. 2(f) and Fig. S8 in the ESM. Moreover, it should be noted that inconspicuous green emissions with EL peak centered at 521 nm can also be detected at high voltages in device R/G. The appearance of green emission in R/G device implies that slight proportion of recombination occurred in $CsPbBr_3$ layer under high voltages. Above all, red emissions from $CsPbI_3$ NCs dominate the EL emissions whether in G/R or R/G type devices. Meanwhile, the superior device performance illustrates that G/R type device is more suitable for multicolor LEDs.

In order to further reveal the differences in charge recombination dynamics, corresponding energy level structures of R/G and G/R type devices are carefully investigated. The relative energy levels of valence band (VB) and conduction band (CB) for $CsPbBr_3$ and $CsPbI_3$ NCs are determined through ultraviolet photoelectron spectroscopy (UPS). As shown in Figs. 3(a) and 3(b), through fitting the linear region of the UPS results at high and low binding energy side, the energy levels of CB and VB for $CsPbBr_3$ are 3.44 and 5.81 eV while CB of 3.64 eV and VB of 5.52 eV are determined for $CsPbI_3$. The energy levels of other layers are widely recognized in Refs. [47, 48]. Using above results, the corresponding energy diagrams of R/G and G/R type devices are illustrated in Figs. 3(c) and 3(d). It can be found that $CsPbBr_3$ NCs possess a lower VB and higher CB level compared to $CsPbI_3$ NCs. Theoretically, the generation of type I quantum well structure between $CsPbBr_3$ and $CsPbI_3$ NCs is conducive to increasing the carrier recombination in $CsPbI_3$ NCs to a certain degree, especially in R/G structure with $CsPbI_3$ NCs directly contacted to TPBi. [49–51]. However, device R/G exhibits a much lower EQE (< 0.01%) compared to device G/R (see Fig. S8 in the ESM), which indicates that the blocking effect of PMMA originating from its insulation nature also plays a vital role in carrier recombination. The varied tunneling effect of electrons

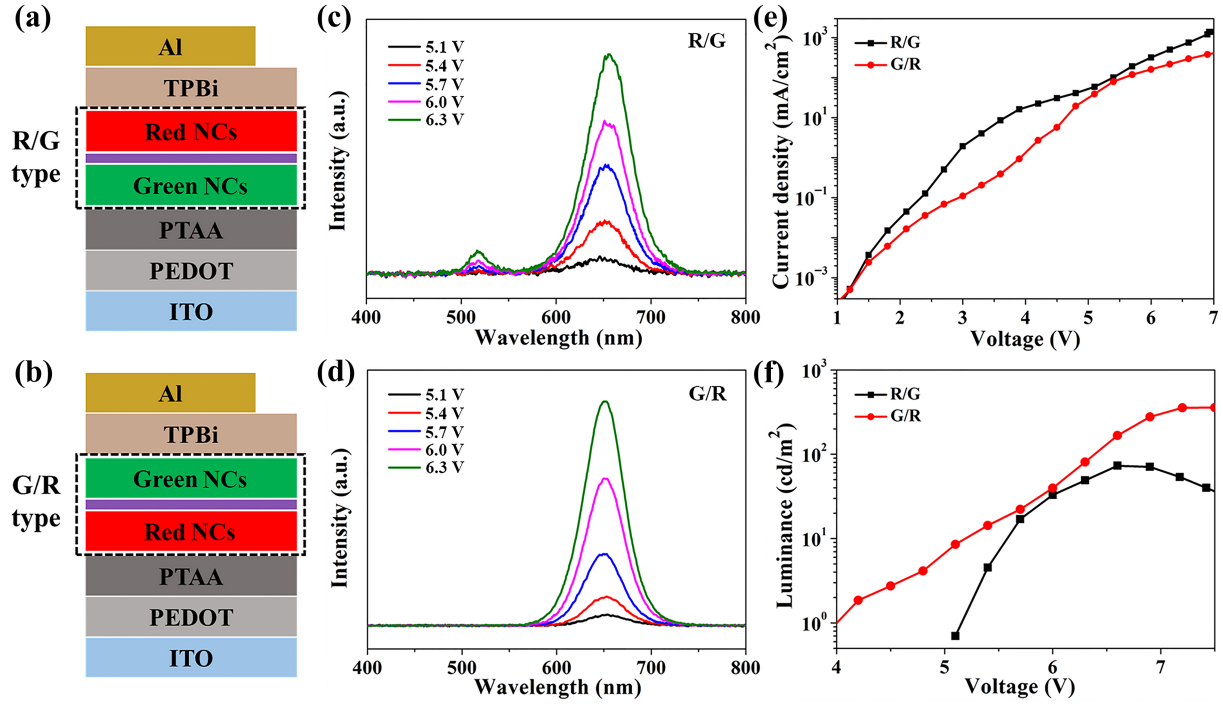

Figure 2 Exploration on EL devices with stacked emission layers. (a) and (b) Device structures of R/G and G/R type devices. (c) and (d) EL emission spectra of R/G and G/R type devices under varied voltages. (e) *J*–*V* curves and (f) *L*–*V* curves of R/G and G/R type devices.

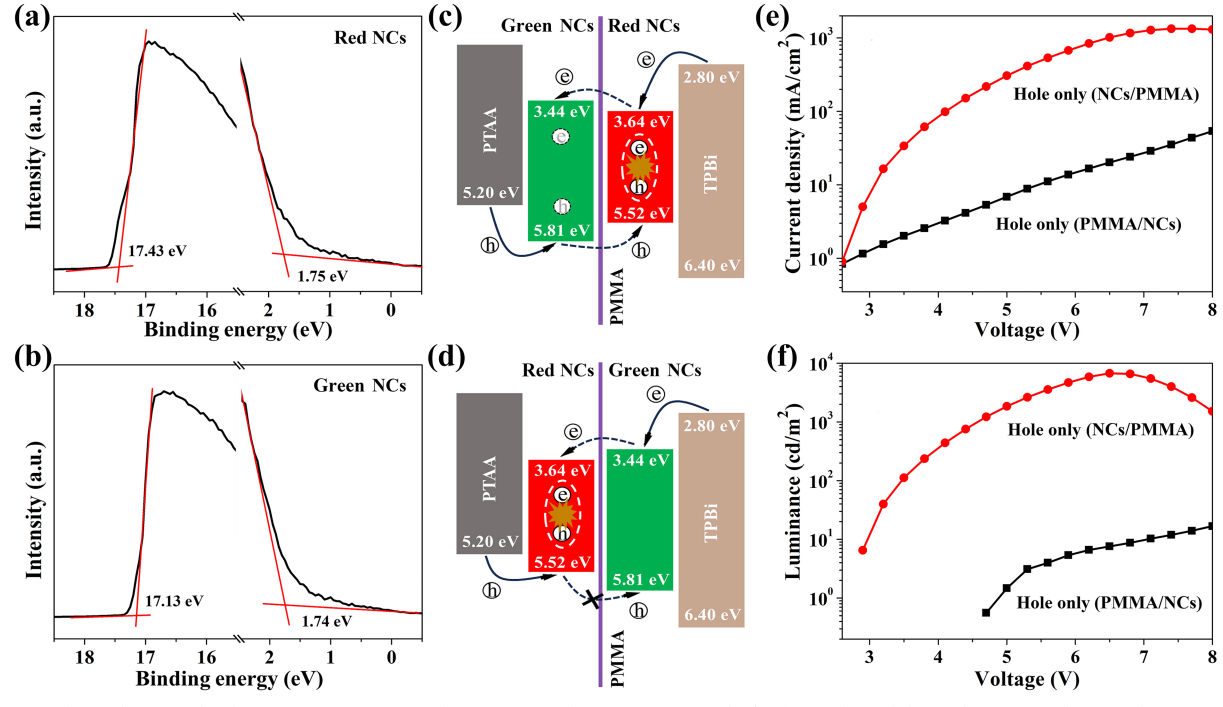

Figure 3 Understanding into the charge carrier injection and transportation dynamics. UPS results for (a) $CsPbI_3$ and (b) $CsPbBr_3$ NCs. Schematic diagrams of energy level structures for devices (c) R/G and (d) G/R. (e) *J*–*V* curves and (f) *L*–*V* curves for devices NCs/PMMA and PMMA/NCs.

and holes through PMMA is further investigated based on hole-only and electron-only devices, as shown in Figs. 3(e) and 3(f) and Fig. S9 in the ESM. For hole-only device, the sequence of $CsPbBr_3$ NCs and PMMA is exchanged with device configuration of ITO/PEDOT/PTAA/NCs/PMMA/4,4′-N,N′-dicarbazolylbiphenyl (CBP)/Al and ITO/PEDOT/PTAA/PMMA/NCs/CBP/Al (derived as NCs/PMMA and PMMA/NCs, respectively). It can be found that the current density of device NCs/PMMA is almost two orders of magnitude larger than that of device PMMA/NCs within operation region (voltage range from 3.5 to 7 V). Besides, device NCs/PMMA exhibits a lower turn-on voltage and maximum luminance of 7000 cd/m^2, while maximum luminance of only 20 cd/m^2 is obtained for device PMMA/NCs. For this hole-only device, electrons are injected through Al side, and holes are injected through ITO side. The dramatically decreased current density and luminance of device PMMA/NCs indicate that the injection and

transportation of holes are greatly hindered by existence of PMMA. On the contrary, the injection and transportation of electrons to NCs are slightly affected when PMMA is located on top of NCs. Analysis on electron-only device also demonstrates that PMMA exhibits a much stronger suppression on holes rather than electrons (see Fig. S9 in the ESM). Based on above analysis, the carrier injection and transportation dynamics can be schematically described in Figs. 3(c) and 3(d). The injected holes can hardly pass through the PMMA layer due to the strong suppression effect of PMMA. Therefore, recombinations of electrons and holes are mainly occurred in $CsPbI_3$ NCs in G/R type device, leading to dominant red emissions. However, under coexistence of strong suppression and quantum well effect in R/G type device, only a few of holes could be injected into $CsPbI_3$ layer. Meanwhile, a few of electrons could also pass through the PMMA layer, giving rise to green emission of $CsPbBr_3$ NCs. As a result, red emission with low luminance and accompanying weak green emission are observed in R/G type device.

The dominant red emissions in EL devices with bilayered $CsPbI_3$ and $CsPbBr_3$ NCs provide great convenience for fabrication of multicolor LEDs without multiple processing steps and further alignment. As device structure shows in Fig. 4(a), G/R type device structure is applied and modified for multicolor EL devices. In this device structure, only $CsPbI_3$ NCs film is processed into striped pixels pattern under fs laser ablation. The stripe width is varied from 10 to 30 μm (with PPI varied from 1693 to 462), derived as devices 10, 15, 20, and 30. Because of the complete removal of $CsPbI_3$ NCs after fs laser processing, $CsPbBr_3$ NCs located on top of the treated area of $CsPbI_3$ would directly contact with the transport layer. In this way, simultaneous green and red emissions during device operation can be accomplished. As *J*–*V* curves show in Fig. 4(b), the current density increases rapidly with bias increasing, demonstrating well carrier injection and transportation characteristics for all the devices. A turn-on voltage of 2.7 V can be identified in *L*–*V* curves shown in Fig. 4(c). With voltage increasing, the luminance also increases with a maximum luminance of 488 cd/m^2 achieved in device 10. To verify the color characteristics of the as-fabricated devices, the EL spectra and photographs of devices under operation condition are captured through spectrometer and confocal microscope. As shown in Fig. 4(d), well defined red and green luminescent stripes with distinct boundaries are observed for all the devices. The width of observed pixelated luminescent stripes is in good agreement with the designed working area for $CsPbBr_3$ and $CsPbI_3$ NCs, which demonstrates that the high resolution nature of NCs film is well maintained in as-fabricated multicolor devices. Dual EL emissions centered at 520 and 660 nm, which are consistent with PL of $CsPbBr_3$ and $CsPbI_3$ NCs, can be clearly identified in EL spectra shown in Fig. 4(e). Moreover, as displayed in Fig. 4(f), these multicolor EL devices exhibit high efficiency with a maximum EQE of 7.7% achieved in device 15. Detailed device operation parameters are also summarized in Table S1 in the ESM. The fluctuation of EQE with resolution may be related with the varied film roughness and current leakage as pixel size varies [38, 52]. Further research is needed to reveal the intrinsic relationship between pixel size and device efficiency. The demonstration of pixelated multicolor EL devices through one-step fs laser ablation may be further applied for realization of high-resolution full color LEDs.

3 Conclusion

In conclusion, high-resolution and multicolor EL devices with red and green pixels are fabricated through fs laser ablation on perovskite NCs film. The fast removal of perovskite NCs in fs laser spot, which is proved by elemental analysis, well clarifies the mechanism of fs laser ablation. By further controlling the scanning route of fs laser, varied patterned $CsPbBr_3$ and $CsPbI_3$ NCs films can be fabricated, especially the obtaining of pixelated $CsPbBr_3$ NCs film with PPI up to 1693. Then, through exploration on prototype EL devices with two emission layers of $CsPbBr_3$ and $CsPbI_3$ NCs, dominant red emissions are demonstrated in G/R or R/G type device. The superior recombination of electrons and holes in $CsPbI_3$

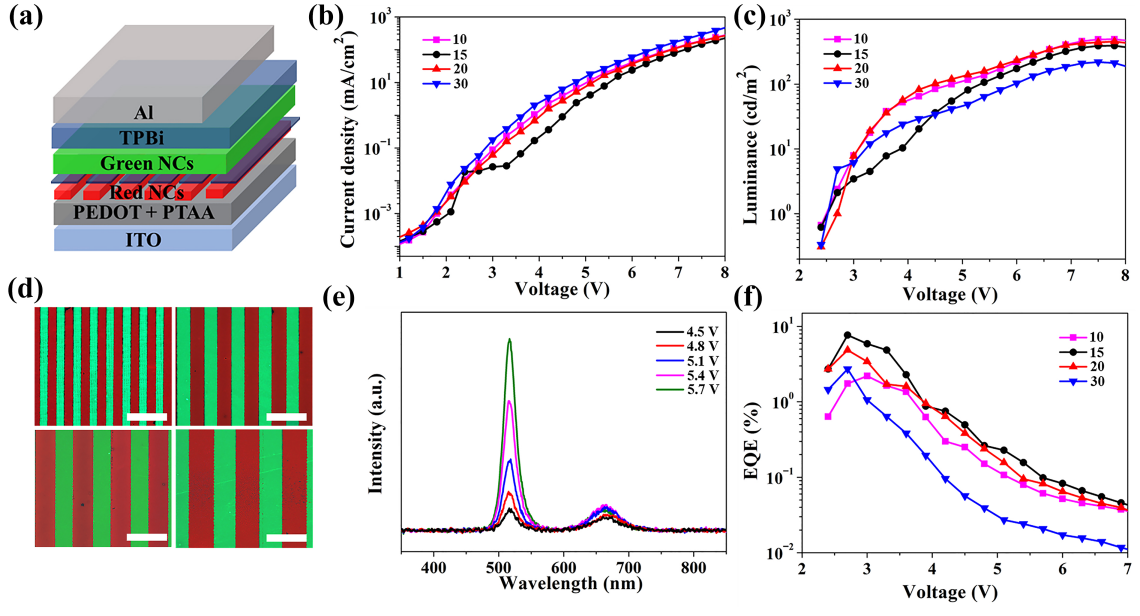

Figure 4 Multicolor EL devices based on perovskite NCs. (a) Device structure of multicolor EL device. (b) *J*–*V* curves and (c) *L*–*V* curves of devices 10, 15, 20, and 30. (d) Microscopy images of devices 10, 15, 20, and 30 during operation. The scale bar is 50 μm. (e) EL spectra of devices 10, 15, 20, and 30 under varied voltages. (f) EQE curves of devices 10, 15, 20, and 30.

NCs is further revealed by the strong suppression effect of PMMA on holes. Owing to this dominant emission from $CsPbI_3$ NCs, multicolor EL devices can be conveniently accomplished with fs laser ablation only conducted on $CsPbI_3$ NCs layer. Finally, multicolored EL emissions originated from green and red pixels with maximum luminance of 488 cd/m^2 and EQE of 7.7% are obtained in as-fabricated EL devices. Our achievement of pixelated multicolor EL devices through fs laser ablation without multiple steps and further alignment may provide an alternative route towards high-resolution full color LEDs and bring more opportunities for development and commercialization of PeQDs based display technologies.

Electronic Supplementary Material: Supplementary material (experimental section, XRD patterns of as fabricated NCs, corresponding TEM images, absorption and PL spectra, microscope images of NCs films after fs laser radiation, device performance of pure red and pure green LEDs, analysis on electron-only devices, detailed device operation parameters, etc.) is available in the online version of this article at https://doi.org/10.26599/NR.2026.94908488.

Data availability

All data needed to support the conclusions in the paper are presented in the manuscript and the ESM. Additional data related to this paper may be requested from the corresponding author upon request.

Acknowledgements

This study was supported by the National Natural Science Foundation of China (Nos. 52303219 and 62375007), Beijing Postdoctoral Research Foundation (No. 2023-zz-53), and Applied Basic Research Fund of the School of Physics and Optoelectronic Engineering, Beijing University of Technology (No. 056000513103).

Declaration of competing interest

All the contributing authors report no conflict of interests in this work.

Author contribution statement

Z. L. L.: Data curation, methodology, validation, software. F. Z.: Experimental design, writing manuscript, validation, supervision, project administration. Z. H. R.: Formal analysis, investigation, visualization. Y. X. Z.: Investigation, data curation, software. T. R. Z.: Project administration, funding acquisition, supervision, review, and editing. All the authors have approved the final manuscript.

Use of AI statement

None.

References

[1] Shirasaki, Y.; Supran, G. J.; Bawendi, M. G.; Bulović, V. Emergence of colloidal quantum-dot light-emitting technologies. *Nat. Photonics* **2013**, *7*, 13–23.

[2] Kagan, C. R.; Lifshitz, E.; Sargent, E. H.; Talapin, D. V. Building devices from colloidal quantum dots. *Science* **2016**, *353*, aac5523.

[3] Fakharuddin, A.; Gangishetty, M. K.; Abdi-Jalebi, M.; Chin, S. H.; bin Mohd Yusoff, A. R.; Congreve, D. N.; Tress, W.; Deschler, F.; Vasilopoulou, M.; Bolink, H. J. Perovskite light-emitting diodes. *Nat. Electronics* **2022**, *5*, 203–216.

[4] Cho, H.; Jeong, S. H.; Park, M. H.; Kim, Y. H.; Wolf, C.; Lee, C. L.; Heo, J. H.; Sadhanala, A.; Myoung, N.; Yoo, S. et al. Overcoming the electroluminescence efficiency limitations of perovskite light-emitting diodes. *Science* **2015**, *350*, 1222–1225.

[5] Alivisatos, A. P. Semiconductor clusters, nanocrystals, and quantum dots. *Science* **1996**, *271*, 933–937.

[6] Yin, Y. D.; Alivisatos, A. P. Colloidal nanocrystal synthesis and the organic–inorganic interface. *Nature* **2005**, *437*, 664–670.

[7] Kovalenko, M. V.; Protesescu, L.; Bodnarchuk, M. I. Properties and potential optoelectronic applications of lead halide perovskite nanocrystals. *Science* **2017**, *358*, 745–750.

[8] Kim, Y. H.; Park, J.; Kim, S.; Kim, J. S.; Xu, H. X.; Jeong, S. H.; Hu, B.; Lee, T. W. Exploiting the full advantages of colloidal perovskite nanocrystals for large-area efficient light-emitting diodes. *Nat. Nanotechnol.* **2022**, *17*, 590–597.

[9] Zhang, F.; Zhong, H. Z.; Chen, C.; Wu, X. G.; Hu, X. M.; Huang, H. L.; Han, J. B.; Zou, B. S.; Dong, Y. P. Brightly luminescent and color-tunable colloidal $CH_3NH_3PbX_3$ (X = Br, I, Cl) quantum dots: Potential alternatives for display technology. *ACS Nano* **2015**, *9*, 4533–4542.

[10] Protesescu, L.; Yakunin, S.; Bodnarchuk, M. I.; Krieg, F.; Caputo, R.; Hendon, C. H.; Yang, R. X.; Walsh, A.; Kovalenko, M. V. Nanocrystals of cesium lead halide perovskites ($CsPbX_3$, X = Cl, Br, and I): Novel optoelectronic materials showing bright emission with wide color gamut. *Nano Lett.* **2015**, *15*, 3692–3696.

[11] Song, J. Z.; Li, J. H.; Xu, L. M.; Li, J. H.; Zhang, F. J.; Han, B. N.; Shan, Q. S.; Zeng, H. B. Room-temperature triple-ligand surface engineering synergistically boosts ink stability, recombination dynamics, and charge injection toward EQE-11.6% perovskite QLEDs. *Adv. Mater.* **2018**, *30*, 1800764.

[12] Li, X. M.; Yu, D. J.; Cao, F.; Gu, Y.; Wei, Y.; Wu, Y.; Song, J. Z.; Zeng, H. B. Healing all-inorganic perovskite films via recyclable dissolution–recyrstallization for compact and smooth carrier channels of optoelectronic devices with high stability. *Adv. Funct. Mater.* **2016**, *26*, 5903–5912.

[13] Lian, Y. X.; Wang, Y. X.; Yuan, Y. C.; Ren, Z. X.; Tang, W. D.; Liu, Z.; Xing, S. Y.; Ji, K. Y.; Yuan, B.; Yang, Y. C. et al. Downscaling micro-and nano-perovskite LEDs. *Nature* **2025**, *640*, 62–68.

[14] Tan, Z. K.; Moghaddam, R. S.; Lai, M. L.; Docampo, P.; Higler, R.; Deschler, F.; Price, M.; Sadhanala, A.; Pazos, L. M.; Credgington, D. et al. Bright light-emitting diodes based on organometal halide perovskite. *Nat. Nanotechnol.* **2014**, *9*, 687–692.

[15] Peng, C. C.; Zhang, R.; Chen, H. T.; Liu, Y.; Zhang, S.; Fang, T.; Guo, R. D.; Zhang, J. B.; Shan, Q. S.; Jin, Y. Z. et al. A demulsification–crystallization model for high-quality perovskite nanocrystals. *Adv. Mater.* **2023**, *35*, 2206969.

[16] Feng, S. C.; Shen, Y.; Hu, X. M.; Su, Z. H.; Zhang, K.; Wang, B. F.; Cao, L. X.; Xie, F. M.; Li, H. Z.; Gao, X. Y. et al. Efficient and stable red perovskite light-emitting diodes via thermodynamic crystallization control. *Adv. Mater.* **2024**, *36*, 2410255.

[17] López-Fernández, I.; Valli, D.; Wang, C. Y.; Samanta, S.; Okamoto, T.; Huang, Y. T.; Sun, K.; Liu, Y.; Chirvony, V. S.; Patra, A. et al. Lead-free halide perovskite materials and optoelectronic devices: Progress and prospective. *Adv. Funct. Mater.* **2024**, *34*, 2307896.

[18] Dai, X. L.; Deng, Y. Z.; Peng, X. G.; Jin, Y. Z. Quantum-dot light-emitting diodes for large-area displays: Towards the dawn of commercialization. *Adv. Mater.* **2017**, *29*, 1607022.

[19] Kim, B. H.; Onses, M. S.; Lim, J. B.; Nam, S.; Oh, N.; Kim, H.; Yu, K. J.; Lee, J. W.; Kim, J. H.; Kang, S. K. et al. High-resolution patterns of quantum dots formed by electrohydrodynamic jet printing for light-emitting diodes. *Nano Lett.* **2015**, *15*, 969–973.

[20] Ahn, J.; Jeon, S.; Woo, H. K.; Bang, J.; Lee, Y. M.; Neuhaus, S. J.;

Lee, W. S.; Park, T.; Lee, S. Y.; Jung, B. K. et al. Ink-lithography for property engineering and patterning of nanocrystal thin films. *ACS Nano* **2021**, *15*, 15667–15675.

[21] Zhang, P. P.; Yang, G. L.; Li, F.; Shi, J. B.; Zhong, H. Z. Direct *in situ* photolithography of perovskite quantum dots based on photocatalysis of lead bromide complexes. *Nat. Commun.* **2022**, *13*, 6713.

[22] Liu, D.; Weng, K. K.; Lu, S. Y.; Li, F.; Abudukeremu, H.; Zhang, L. P.; Yang, Y. C.; Hou, J. Y.; Qiu, H. W.; Fu, Z. et al. Direct optical patterning of perovskite nanocrystals with ligand cross-linkers. *Sci. Adv.* **2022**, *8*, eabm8433.

[23] Choi, M. K.; Yang, J.; Kang, K.; Kim, D. C.; Choi, C.; Park, C.; Kim, S. J.; Chae, S. I.; Kim, T. H.; Kim, J. H. et al. Wearable red-green-blue quantum dot light-emitting diode array using high-resolution intaglio transfer printing. *Nat. Commun.* **2015**, *6*, 7149.

[24] Kim, L.; Anikeeva, P. O.; Coe-Sullivan, S. A.; Steckel, J. S.; Bawendi, M. G.; Bulović, V. Contact printing of quantum dot light-emitting devices. *Nano Lett.* **2008**, *8*, 4513–4517.

[25] Meng, T. T.; Zheng, Y. T.; Zhao, D. L.; Hu, H. L.; Zhu, Y. B.; Xu, Z. W.; Ju, S. M.; Jing, J. P.; Chen, X.; Gao, H. J. et al. Ultrahigh-resolution quantum-dot light-emitting diodes. *Nat. Photonics* **2022**, *16*, 297–303.

[26] Zhang, Z. X.; Li, Z. R.; Chen, Y. F.; Zhang, Z. J.; Fan, K.; Chen, S. Y.; Liu, L. H.; Chen, S. F. Progress on inkjet printing technique for perovskite films and their optoelectronic and optical applications. *ACS Photonics* **2023**, *10*, 3435–3450.

[27] Singh, M.; Haverinen, H. M.; Dhagat, P.; Jabbour, G. E. Inkjet printing—process and its applications. *Adv. Mater.* **2010**, *22*, 673–685.

[28] Xiao, Z.; Zhang, M.; Ding, Y. H.; Shi, Z. Y.; Yin, Z. H.; Deng, H. H.; Meng, L. L.; Xu, B. J.; Liu, H. Solution-processed quantum dot micropatterns: From liquid manipulation to high-performance quantum dot light-emitting diode devices. *ACS Nano* **2025**, *19*, 10609–10619.

[29] Li, Z. Z.; Fan, H.; Wang, L.; Zhang, X.; Zhao, X. J.; Yu, Y. H.; Xu, Y. S.; Wang, Y.; Wang, X. J.; Juodkazis, S. et al. Super-stealth dicing of transparent solids with nanometric precision. *Nat. Photonics* **2024**, *18*, 799–808.

[30] Liang, S. Y.; Liu, Y. F.; Ji, Z. K.; Wang, S. Y.; Xia, H.; Sun, H. B. High-resolution patterning of perovskite quantum dots via femtosecond laser-induced forward transfer. *Nano Lett.* **2023**, *23*, 3769–3774.

[31] Shin, S. Review of high-precision femtosecond laser materials processing for fabricating microstructures: Effects of laser parameters on processing quality, ablation efficiency, and microhole shape. *J. Laser Appl.* **2024**, *36*, 041201.

[32] Ancona, A.; Döring, S.; Jauregui, C.; Röser, F.; Limpert, J.; Nolte, S.; Tünnermann, A. Femtosecond and picosecond laser drilling of metals at high repetition rates and average powers. *Opt. Lett.* **2009**, *34*, 3304–3306.

[33] Sun, K.; Tan, D. Z.; Fang, X. Y.; Xia, X. T.; Lin, D. J.; Song, J.; Lin, Y. H.; Liu, Z. J.; Gu, M.; Yue, Y. Z. et al. Three-dimensional direct lithography of stable perovskite nanocrystals in glass. *Science* **2022**, *375*, 307–310.

[34] Huang, X. J.; Guo, Q. Y.; Yang, D. D.; Xiao, X. D.; Liu, X. F.; Xia, Z. G.; Fan, F. J.; Qiu, J. R.; Dong, G. P. Reversible 3D laser printing of perovskite quantum dots inside a transparent medium. *Nat. Photonics* **2020**, *14*, 82–88.

[35] Zhang, Y. N.; Zhu, S. T.; Hu, J. M.; Gu, M. Femtosecond laser direct nanolithography of perovskite hydration for temporally programmable holograms. *Nat. Commun.* **2024**, *15*, 6661.

[36] Jia, Y. C.; Chen, F. Recent progress on femtosecond laser micro-/nano-fabrication of functional photonic structures in dielectric crystals: A brief review and perspective. *APL Photonics* **2023**, *8*, 090901.

[37] Nie, L.; Wang, T.; Yu, X.; Gao, W.; Peng, Q. P.; Xia, Z. G.; Qiu, J. B.; Yu, S. F.; Xu, X. H. Multicolor display fabricated via stacking CW laser-patterned perovskite films. *ACS Energy Lett.* **2023**, *8*, 2025–2032.

[38] Ma, T.; Wang, Y. F.; Chen, J.; Wang, R.; Lv, R. Q.; Chen, Z. Y.; Guo, W. S.; Guo, T. T.; Ji, Y. C.; Song, X. F. et al. One-step, mask-free, rapid laser writing fabrication of electroluminescent perovskite@oxide pixels for ultra-high PPI, efficient micro-QLEDs. *Adv. Funct. Mater.* **2025**, *35*, 2413811.

[39] Ghasemi, M.; Guo, B. Y.; Darabi, K.; Wang, T. H.; Wang, K.; Huang, C. W.; Lefler, B. M.; Taussig, L.; Chauhan, M.; Baucom, G. et al. A multiscale ion diffusion framework sheds light on the diffusion-stability-hysteresis nexus in metal halide perovskites. *Nat. Mater.* **2023**, *22*, 329–337.

[40] Yuan, Y. B.; Huang, J. S. Ion migration in organometal trihalide perovskite and its impact on photovoltaic efficiency and stability. *Acc. Chem. Res.* **2016**, *49*, 286–293.

[41] Zhang, F.; Zhang, X.; Wang, C. H.; Sun, M. N.; Luo, X. Y.; Yang, Y. G.; Chang, S.; Zhang, D. D.; Duan, L. Chlorine distribution management for spectrally stable and efficient perovskite blue light-emitting diodes. *Nano Energy* **2021**, *79*, 105486.

[42] Karlsson, M.; Yi, Z. Y.; Reichert, S.; Luo, X. Y.; Lin, W. H.; Zhang, Z. Y.; Bao, C. X.; Zhang, R.; Bai, S.; Zheng, G. H. J. et al. Mixed halide perovskites for spectrally stable and high-efficiency blue light-emitting diodes. *Nat. Commun.* **2021**, *12*, 361.

[43] Li, G. J.; Tseng, M. C.; Chen, Y.; Yeung, F. S. Y.; He, H. Y.; Cheng, Y. C.; Cai, J. H.; Chen, E. G.; Kwok, H. S. Color-conversion displays: Current status and future outlook. *Light Sci. Appl.* **2024**, *13*, 301.

[44] Shim, H. C.; Kim, J.; Park, S. Y.; Kim, B. S.; Jang, B.; Lee, H. J.; Kim, A.; Hyun, S.; Kim, J. H. Full-color micro-LED display with photo-patternable and highly ambient-stable perovskite quantum dot/siloxane composite as color conversion layers. *Sci. Rep.* **2023**, *13*, 4836.

[45] Ko, J.; Ma, K.; Joung, J. F.; Park, S.; Bang, J. Ligand-assisted direct photolithography of perovskite nanocrystals encapsulated with multifunctional polymer ligands for stable, full-colored, high-resolution displays. *Nano Lett.* **2021**, *21*, 2288–2295.

[46] Lin, K. B.; Xing, J.; Quan, L. N.; de Arquer, F. P. G.; Gong, X. W.; Lu, J. X.; Xie, L. Q.; Zhao, W. J.; Zhang, D.; Yan, C. Z. et al. Perovskite light-emitting diodes with external quantum efficiency exceeding 20 per cent. *Nature* **2018**, *562*, 245–248.

[47] Lu, M.; Zhang, Y.; Wang, S. X.; Guo, J.; Yu, W. W.; Rogach, A. L. Metal halide perovskite light-emitting devices: Promising technology for next-generation displays. *Adv. Funct. Mater.* **2019**, *29*, 1902008.

[48] Fan, G. T.; Zhang, F.; Lu, Z. L.; Ren, Z. H.; Zhai, T. R. Tuning the triplet state of ligands on $FAPbBr_3$ quantum dots toward low-threshold distributed feedback lasers. *J. Phys. Chem. Lett.* **2025**, *16*, 5674–5680.

[49] Jiang, Y. Z.; Wei, J. L.; Yuan, M. J. Energy-funneling process in quasi-2D perovskite light-emitting diodes. *J. Phys. Chem. Lett.* **2021**, *12*, 2593–2606.

[50] Xu, B.; Yuan, S. C.; Wang, L. Q.; Li, X. S.; Hu, Z.; Zeng, H. B. Highly efficient blue light-emitting diodes enabled by gradient core/shell-structured perovskite quantum dots. *ACS Nano* **2025**, *19*, 3694–3704.

[51] Lei, L.; Seyitliyev, D.; Stuard, S.; Mendes, J.; Dong, Q.; Fu, X. Y.; Chen, Y. A.; He, S. L.; Yi, X. P.; Zhu, L. P. et al. Efficient energy funneling in quasi-2D perovskites: From light emission to lasing. *Adv. Mater.* **2020**, *32*, 1906571.

[52] Jing, Y. Y.; Yao, M. Y.; Yang, M.; Li, M. L.; Ding, H.; Yang, G. L.; Zhang, R. J.; Han, D. B.; Liu, H.; Zhong, H. Z. Photolithographic fabrication of high-resolution Micro-QLEDs towards color-conversion microdisplay. *Light Sci. Appl.* **2025**, *14*, 370.